Biotechnology and Bioengineering

WILEY

BIOTECHNOLOGY AND BIOENGINEERING

ARTICLE OPEN ACCESS

Transferrin Purification, Biophysical Characterization, and Lung Biodistribution in Sickle Cell Disease Mice

Shuwei Lu[1] | Mohd A. Khan[1] | Saini Setua[2] | Quintin O'Boyle[1] | Kiruphagaran Thangaraju[2] | Pedro Cabrales[3] | Delaney C. Swindle[4] | David C. Irwin[4] | Paul W. Buehler[2,3,5] | Andre F. Palmer[1]

[1]William G. Lowrie Department of Chemical and Biomolecular Engineering, College of Engineering, The Ohio State University, Columbus, Ohio, USA | [2]Center for Blood Oxygen Transport and Hemostasis, Department of Pediatrics, University of Maryland School of Medicine, Baltimore, Maryland, USA | [3]Department of Bioengineering, University of California San Diego, La Jolla, California, USA | [4]Cardiovascular and Pulmonary Research Group, Department of Medicine, University of Colorado, Anschutz Medical Campus, Aurora, Colorado, USA | [5]Department of Pathology, University of Maryland School of Medicine, Baltimore, Maryland, USA

Correspondence: Andre F. Palmer (Palmer.351@osu.edu)

Received: 17 February 2025 | **Revised:** 17 June 2025 | **Accepted:** 18 June 2025

Funding: This study was supported by the Grants R01HL162120, HT94252410238, R01HL158076, and R01HL159862.

ABSTRACT

Plasma transferrin (Tf) is the transport protein central to the process of iron recycling and metabolism. Holo-Tf serves as the body's pool of ferric iron, facilitating transport from tissues such as the intestine, liver, spleen, and finally bone marrow, where iron is incorporated into erythropoiesis. In sickle cell disease (SCD), iron overload is primarily caused by chronic blood transfusions in patients at risk of stroke or frequent acute pain crisis. However, we have identified that pulmonary vascular iron accumulation, independent of transfusion, is a driver of pulmonary hypertension in SCD patients and murine models. Therefore, we hypothesize that intra-pulmonary administration of apo-Tf localizes the protein to sites of iron accumulation within the lung, where reactive iron-driven pathology develops. This approach to therapeutic development focuses on optimizing administration using aerosol drug delivery, which can increase clinical compliance compared to subcutaneous or intravenous administration. The goal of this study was to purify apo-Tf using a novel process, perform biochemical characterization on the material, and test the proof of concept that apo-Tf protein can be delivered to lung regions where iron accumulation occurs in SCD pulmonary hypertension. We conclude that apo-Tf can be isolated from plasma Cohn fraction IV paste using a simple process and that characterization of the material identified a high-purity apo-Tf product with functional iron binding properties. Further, this material was administered to SCD mice to target pulmonary anatomical regions where pathology occurs. This data suggests an intriguing approach to iron chelation applicable to a relevant clinical population.

1 | Introduction

Human transferrin (Tf) is a glycoprotein (MW = 79.5 kDa) present in human plasma at concentrations between 2 and 4 mg/mL. Normal Tf iron saturations are typically 20%– 45% in healthy individuals, which accounts for a small portion of the total body iron pool (MacGillivray et al. 1983; Cancado et al. 2008; Elsayed et al. 2016). Nonetheless, Tf recycles all of the iron required for red blood cell production and does so in more than 100 cycles of iron binding and delivery (Hentze et al. 2004). The C- and N-lobe pockets of the Tf protein bind one ferric iron (Fe^{3+}) atom each (Anderson et al. 1989; Wally et al. 2006), and Tf circulates in plasma as apo-Tf, mono-ferric-Tf, and di-ferric (holo-Tf). Holo-Tf binds to cell surface Tf receptor 1 (TfR1), creating a receptor–ligand complex with TfR1 and two holo-Tf proteins that initiates cellular iron utilization as well as recycling of apo-Tf (Wally et al. 2006; Ginzburg et al. 2023). Further, Tf's function allows for the prevention of iron's unwanted distribution and excess

accumulation in tissues as well as iron's participation in unwanted oxidation reactions that contribute toward tissue damage (Jackson and Morris 1961).

We have identified a unique iron accumulation in adventitial macrophages surrounding pre- and post-capillary pulmonary vessels of patients and murine models of SCD pulmonary hypertension (Buehler et al. 2021; Redinus et al. 2019). Because iron accumulation is specific to the lung vasculature in SCD pulmonary hypertension, targeting the lungs with aerosolized Tf is a potential approach to therapeutic intervention. In this situation, labile or reactive iron in localized tissue parenchymal compartments facilitates protein and lipid peroxidation (Bacon et al. 1983), senescence, fibrosis, and contributes to cardiopulmonary dysfunction (Smith et al. 1997; Britton 1994). We suggest that macrophage iron loading leads to excess transport of iron through ferroportin and that labile iron contributes toward pulmonary vascular remodeling and pulmonary hypertension in SCD. In support of this pathophysiological concept, Tf receptor 2 gene-deficient and homeostatic iron regulator gene-deficient mice show pulmonary iron accumulation, airway fibrosis, and lung functional decline (Ali et al. 2020). In these preclinical models, iron chelators given by the intranasal route attenuate markers of fibrosis. In the distal lung, Tf functions as an antioxidant, but pulmonary Tf concentrations are decreased in the lung lavage fluid from patients with chronic obstructive pulmonary disease (Stites et al. 1995). SCD patients with low serum Tf concentrations (< 1.6 mg/mL, normal 2–3 mg/mL) are reported to have higher tricuspid regurgitant jet velocity (an indicator of pulmonary hypertension) as well as increased endothelial dysfunction and mortality (Pakbaz et al. 2011). Therefore, we have strategized therapeutic approaches to target pulmonary vascular sites, such as pre- and post-capillary vessels where iron-loaded macrophages accumulate.

Several methods to purify Tf have been developed in the past, using plasma, and various Cohn fractions as the starting material (Leibman and Aisen 1967; Koechlin 1952; Kistler et al. 1960; Inman et al. 1961). Tf purification techniques include ammonium sulfate precipitation (Leibman and Aisen 1967), ethanol precipitation (Koechlin 1952), rivanol precipitation (Kistler et al. 1960), and ion exchange chromatography (IEX) (Inman et al. 1961). Additionally, several methods have been developed to purify Tf using Cohn fractions I to IV (McCann et al. 2005; Ascione et al. 2010; Von Bonsdorff et al. 2001). A patent for the purification of Tf from Cohn fraction IV using PEG and $ZnCl_2$ precipitation before anion exchange chromatography using a weak anion exchanger was active between 1996 and 2016 (Rolf et al. 1996). Recently, Ascione et al. (2010) reported a purification method using a combination of Tween 80 for viral inactivation, followed by dead-end filtration before cassette tangential flow filtration (TFF) and anion exchange chromatography to purify apo-Tf from Cohn fraction IV. The abundance of Tf in plasma makes it a potential source to produce large quantities of Tf. The Cohn plasma fractionation process primarily purifies albumin, and generates various waste fractions (Cohn et al. 1946). For example, Cohn fraction IV is one such waste product of the Cohn fractionation process that contains significant amounts of Tf (Pires et al. 2021). The preparation of apo-Tf by plasma fractionation may offer a novel material that can be delivered to vascularized lung regions to facilitate iron binding and enhance localized antioxidant activity.

The objectives of this study were to optimize a scalable Tf purification process using anion exchange chromatography on a protein cocktail obtained from TFF fractionation of Cohn fraction IV (Pires et al. 2021). Previous studies purifying Tf from Cohn fraction IV required multiple steps for purification such as precipitation and several filtration steps (Inman et al. 1961; Ascione et al. 2010; Von Bonsdorff et al. 2001; Rolf et al. 1996). In this study, we propose a simple and scalable process that only requires TFF for protein separation based on size, followed by IEX with a strong anion exchanger for the purification of apo-Tf. The purified Tf was then analyzed for structural and functional integrity by various biophysical techniques. Preliminary studies in Berkeley SCD mice were then conducted using the novel Tf preparation to determine lung distribution and systemic absorption following intra-pulmonary delivery using a rodent micro-sprayer.

2 | Materials and Methods

2.1 | Materials

Trizma, trizma HCl, sodium chloride, sodium phosphate dibasic, sodium phosphate monobasic, iron chloride (97%), and nitrilotriacetate (99%) were purchased from Sigma Aldrich (St. Louis, MO), while 0.2 μm polyethersulfone syringe filters were purchased from ThermoFisher (Waltham, MA). Human Cohn fraction IV was purchased from Seraplex (Pasadena, CA). All protein purifications were performed using prepacked columns (Cytiva, Marlborough, MA) on an NGC Quest 100 chromatography system (BioRad, Hercules, CA).

2.2 | Tf Purification

Human Cohn fraction IV (FIV) paste was suspended in 3.75 mM phosphate buffered saline (PBS) at 4°C and centrifuged along with fumed silica for lipid removal. The protein solution was then clarified using TFF as previously reported in the literature to yield a protein cocktail bracketed between 50 and 100 kDa (Pires et al. 2021). The protein cocktail was then used as the starting material for Tf purification using a 20 mL HiPrep Q Sepharose FF column (Cytiva, Marlborough, MA). Two buffers, 25 mM Tris, pH 8.00 (buffer A), and 25 mM Tris pH 8.00 containing 0.5 M NaCl (buffer B) were used for binding and eluting protein from the column. The protein cocktail was diluted to a concentration of 25 mg/mL using buffer A and filtered using a 0.2 μm filter before it was loaded onto the column. After completion of protein binding onto the column, the column was then washed with buffer A for five column volumes (CVs). Proteins eluted with increasing concentrations of buffer B at 10%, and 20%. A clean-in-place run was performed between each purification using 2 M NaCl to remove any bound proteins, followed by washing with five CVs of buffer A. Pure Tf fractions were pooled and concentrated using a 50 kDa Amicon ultracentrifuge filter (Millipore Sigma, St. Louis, MO). The purified Tf was treated with 50 mM EDTA overnight at 4°C to remove Tf

bound iron to obtain apo-Tf, followed by buffer exchange into 50 mM phosphate buffer, pH 7.4, using a 50 kDa Amicon ultra centrifuge filter. The protein was concentrated post buffer exchange and stored at −20°C until further use.

2.3 | Total Protein Concentration

Total protein concentration was determined using the Bradford assay (Bradford 1976).

2.4 | SDS-PAGE Analysis

Pre-cast 4%–20% Novex tris-glycine mini protein gels (Invitrogen (Waltham, MA) were used with the Novex mini gel tank (Waltham, MA) for SDS-PAGE analysis. Sodium dodecyl sulfate (SDS) running buffer (10×) was purchased from Invitrogen (Waltham, MA). Samples were diluted to 1 mg/mL in 3.75 mM phosphate buffered saline (PBS) (pH: 7.4) before addition of SDS in a 1:1 ratio and heated at 85°C for 10 min. Twenty microliters of the sample were then loaded onto the gels and ran at 220 V for 40 min. The completed gel was then stained with Coomassie blue (Thermofisher, Waltham, MA) for 40 min and destained overnight using a destaining reagent (60% deionized water, 30% methanol, 10% acetic acid). Densitometric analysis was performed with GelQuantNet software provided by http://biochemlabsolutions.com to determine protein purity.

2.5 | MALDI-TOF Mass Spectrometry

Samples were diluted to 1 mg/mL on a protein basis in 50 mM PB (pH 7.4). A saturated solution of α-cyano-4-hydroxycinnamic acid (CHCA) was prepared for use as the matrix by adding 10 mg of CHCA to 1 mL of 50% v/v acetonitrile with 0.1% trifluoroacetic acid. The sample was prepared by mixing protein, matrix and 1 M HCl in a 1:5:1 ratio. A 1 μL sample was loaded onto a matrix-assisted laser desorption ionization (MALDI) plate. The MALDI plate was then analyzed on a Bruker Microflex MALDI time of flight (MALDI-TOF) mass spectrometry system (Bruker, Billerica, MA). The data was analyzed using the Bruker Flex Analysis software (Bruker, Billerica, MA).

2.6 | Trypsin Digest Mass Spectrometry

Samples were resuspended in 50 mM ammonium bicarbonate solution. Five microliters of dithiothreitol (5 μg/μL in 50 mM ammonium bicarbonate) was added and the sample was incubated at 65°C for 15 min. Post incubation, 5 μL of iodoacetamide (15 mg/mL in 50 mM ammonium bicarbonate) was added and the samples were kept in the dark at room temperature for 30 min. Sequencing grade-modified trypsin (Promega, Madison, WI) was prepared in 50 mM ammonium bicarbonate. The trypsin was added to the sample reaction in a 1:50 (enzyme: sample) ratio at 37°C overnight. The reaction was quenched the following morning by adding formic acid (FA) (50 μL, 0.1%) for acidification. Samples were dried in a SpeedVac (Eppendorf, Enfield, CT) and resuspended in 0.1% FA. The concentration of the resultant peptides was measured by Nanodrop (Fisher, Pittsburgh, PA) before liquid chromatography tandem mass spectrometry (LC/MS-MS) (Fisher, Pittsburgh, PA) analysis. Experiments were performed label-free and the exponentially modified protein abundance index (emPAI) was used to evaluate the relative abundance of individual proteins within a sample (Ishihama et al. 2005). Data analysis was performed using Scaffold 5 (Proteome Software, Portland, OR).

2.7 | UV-Visible Spectroscopy

The ferric Fe binding capacity of the purified Tf was determined by monitoring the reaction of Tf with iron-nitrilotriacetic acid (FeNTA) (Welch and Skinner 1989). The reaction mixture was kept at room temperature overnight on a shaker plate. The absorbance spectra of Tf at 465 nm with and without FeNTA with no additional carbonate added was measured between 350 and 700 nm at 25°C using a Hewlett-Packard 8452A spectrophotometer (HP, Palo Alto, CA). The holo-Tf extinction coefficient of $\mathcal{E}_{465\ \mathrm{nm}} = 4.86\ \mathrm{mM}^{-1}\mathrm{cm}^{-1}$ was used to determine the total amount of active protein (i.e., apo-Tf) (Frieden and Aisen 1980).

2.8 | Circular Dichroism Spectroscopy

The circular dichroism (CD) spectra in the far ultraviolet region between 190 and 260 nm in a 0.1 cm path length quartz cuvette was measured on purified Tf samples using a JASCO J-815 CD spectrometer (Jasco, Easton, Maryland). Samples were diluted to 2 mg/mL (protein basis) in 50 mM phosphate buffer (pH 7.4). Baseline subtraction was performed using 50 mM phosphate buffer (PB), and the protein CD spectra consisted of an average of three scans. Data analysis was performed using Spectra Manager (Jasco, Easton, Maryland).

2.9 | Hemoglobin Auto-Oxidation

Auto-oxidation of human hemoglobin (Hb) was monitored on a Hewlett-Packard 8452A spectrophotometer (HP, Palo Alto, CA). Hb at a concentration of 100 μM was combined with 50 μM FeNTA and 50 μM apo-Tf. The absorbance spectra between 350 and 700 nm were measured at 37°C to determine the ability of apo-Tf to reduce auto-oxidation of Hb in the presence of Fe. The data was regressed to a linear fit in R Studio (Posit, Boston, MA) and the slope was taken as the first-order rate constant for Hb auto-oxidation.

2.10 | Fe Titration

Tf samples were diluted to ~2.9 mg/mL in 50 mM PB (pH 7.4). FeNTA was combined with Tf at concentrations of 10, 20, 30, 40, 50, 60, 65, 70, 75, 80, 85, 90, 100, 110, 120 μM before incubating at 25°C for 1 h. Post incubation, 350 μL of each aliquot were then transferred to a 96-well plate and absorbances at 450 nm were measured on a VersaMax tunable microplate reader (Molecular Devices, San Jose, CA). The data was

regressed to a linear fit in R Studio (Posit, Boston, MA). The intersection of the two lines is indicative of apo-Tf saturation with iron.

2.11 | Fe Binding Kinetics

The binding kinetics between apo-Tf and FeNTA was performed using a SX-20 stopped-flow spectrophotometer (Applied Photophysics, Leatherhead, UK). Purified Tf was diluted to 5 μM, with Fe ligand (i.e., FeNTA) concentrations of 10, 20, 40, 80 μM in 2 mM Tris buffer (pH 7.4) and fluorescence quenching was measured at a wavelength of 285 nm at room temperature. All experiments were performed in triplicate. The data was regressed to a double exponential fit in R Studio (Posit, Boston, MA).

2.12 | Electron Paramagnetic Resonance Spectroscopy

Tf samples were incubated with FeNTA in excess at room temperature while shaking for 2 h before experiments. Four millimeter medium wall Suprasil EPR sample tubes 250 mm L (Wilmad Life Sciences, Vineland, NJ) were used for loading the samples. The holo-Tf sample was then buffer exchanged with 50 mM PB (pH 7.4) twice on a 50 kDa Amicon centrifuge filter. EPR measurements were performed at 20 K using an X-Band (9.4 GHz) EMXPlus (Bruker, Billerica, MA). Temperature control was maintained using a MercuryITC (Oxford Instruments, Oxfordshire, UK). The following settings were used for sample analysis: microwave power 2 mW, receiver gain 30 dB, modulation amplitude 10 G, modulation frequency 100 kHz. The sample was measured at center 2600 G with a sweep width of 4000 G. Five measurements were averaged to reduce noise in the spectra. Data analysis was performed using Xenon (Bruker, Billerica, MA) and EasySpin Documentation on the http://EasySpin.org website.

2.13 | Animal Studies

Berkeley SCD (Berk-SS) mice were obtained from Jackson Laboratories (Bar Harbor, ME, USA). Mice were housed and bred at the University of Maryland Baltimore School of Medicine. Female heterozygous Berk-SS mice were bred with male homozygous Berk-SS mice to generate homozygous offspring. Berk-SS mice with genotype Tg(Hu-miniLCR α1 Gγ Aγ δ βs) Hba0/0 Hbb0/0 and hemizygous with genotype Tg(Hu-miniLCR α1 Gγ Aγ δ βs) Hba0/0 Hbb0 Hbb+ were littermates. Genotyping of mice used for breeding and experiments was performed by TransnetYX (Cordova, TN, USA). All experimental procedures were conducted under the guidelines recommended by the National Institutes of Health and were approved by the Institutional Animal Care and Use Committees at the University of Maryland Baltimore School of Medicine and the University of Colorado Anschutz Medical Campus.

Tf was dosed by aerosolized intrapulmonary delivery in $N = 28$ mice (mixed male and female). Mice were lightly anesthetized with isoflurane (3%–4%), and then placed in the prone position with the mouth open and the vocal cords visualized. The tip of the Penn-Century micro-sprayer was inserted through the middle of the two vocal cords into the upper trachea. The protein was given as a 300 mg/kg dose in 0.9% sodium chloride (~ 200 μL) and was aerosolized through the micro-sprayer tip. The rationale for this dose was based on our previous work with human Tf in beta thalassemia $Hbbth^{3/+}$ mice, where 300 mg/kg was given through the intraperitoneal route daily for 30 days (Gelderman et al. 2015). This dose was used to determine Tf absorption from the lung and subcutaneous absorption. Further, for this study, intraperitoneal administration was not considered to be a translationally relevant route of administration. The procedure lasted 3–5 s and animals were observed until fully awake and alert and moving normally about their cages. Dosing was performed daily for 5 days and after the final dose, animals were allocated to pre- and post-dosing groups at 1, 2, 4, 8, 12, 24 h ($N = 4$/time point) for blood collection and lung tissue harvesting. Under isoflurane (4%), blood was collected from the right ventricle into 1 mL lithium heparin tubes (Greiner Bio-One GmbH, Austria). The aorta was severed, and the lungs were perfused of remaining blood with PBS (5 mL) through the right ventricle. Lung fixation was performed with 10% buffered formalin (3 mL) by airway inflation under constant pressure at 25 cm of H_2O pressure, after which the lungs were removed. Blood was processed to plasma for analysis of endogenous murine and dosed human Tf. In a second set of mice, Tf was dosed by subcutaneous injection ($N = 28$ mice, mixed male, and female). The protein was given as a 300 mg/kg dose in 0.9% sodium chloride (~ 200 μL) for 5 days. After the final dose, animals were allocated to pre- and post-dosing groups at 1, 2, 4, 8, 12, 24 h ($N = 4$/time point) for blood collection and processing as stated previously. Analysis of lung distribution was performed on lung samples before treatment (NT) and at 2, 4, 8, 12 and 24 h post dosing. Plasma concentrations were analyzed for pre- and post-dosing groups at 1, 2, 4, 8, 12, 24 h to determine if Tf was absorbed from the lung following intrapulmonary dosing. AUCs of plasma concentrations versus time were used to determine bioavailability (%F) using the formula ($\%F = AUC_{\text{intra-pulmonary}} / AUC_{\text{subcutaneous}} \times 100$). Here, we evaluated Berk-SS mice rather than background wild-type mice (C57BL/6) with specific interest in assessing disease state biodistribution and pharmacokinetics. This is further rationalized by the development path for SCD therapeutics where Phase I trials to assess pharmacokinetics, biodistribution, and safety are often conducted on patients rather than healthy volunteers (Howard et al. 2019; Misra et al. 2017; Shore et al. 2024).

2.14 | Tissue and Plasma Analysis

Whole lung clearing and imaging: Berk-SS mice were dosed by aerosolized intra-pulmonary administration with 300 mg/kg Alexa Fluor 647 conjugated Tf derived from human serum (Alexa Fluor 647 Conjugate, Cat # T23366) for 5 days. Blood was collected from the heart, and mice were euthanized 10 min after the final dose. The lungs were perfused with 5 mL saline and 1 mL of 4% PFA through the trachea to maintain the lung structure. Lungs were removed and fixed in cold 4% PFA overnight at 4°C. Post-fixed lungs were washed in PBS three times, and the PBS was changed every 2 h. Further, the lunges were transferred into Cubic-L at 37°C and the solution was

replaced with fresh Cubic-L (TCI, T3740) every 2 days until the lobes were uniformly opaque (total of 3–4 days). After Cubic-L clearance, the lungs were transferred to a small amount of Cubic-R + (M) (TCI, T3741) and gently shaken to remove most of the Cubic-L and move into fresh Cubic-R + (M). Lungs were incubated in Cubic-R + (M) at room temperature for 2 days or until the lobes were transparent. Bondic glue was used on the flat surface of the sample holder, and the lung lobes were fixed on the sample holder and UV light was used to dry the glue on the sample and the sample holder. The sample chamber was filled with Cubic-R + (M), and the sample holder with the sample was placed into the chamber for imaging. A Lightsheet 7 microscope and ZEN 3.1 (Black edition) software were used to image and analyze whole lungs. To identify autofluorescence, the samples were excited with a 488 nm laser, and to detect Alexa Fluor 647, the samples were excited with a 638 nm laser. Image analysis was performed using Arivis Vision4D 3.5.0 software.

Lung Immunofluorescence: Formalin-fixed tissue sections from Berk-SS mice dosed with apo-Tf (300 mg/kg) purified from human Cohn fraction IV paste were processed for immunofluorescence (Lamb et al. 2023). Briefly, sections were then incubated (overnight, 4°C). Tf immunofluorescence was performed using an anti-Tf primary antibody (Proteintech, #17435-1-AP) with an anti-Rabbit IgG (H + L) followed by a secondary antibody with Alexa flourTM647 for 1 h. The sections were then washed three times and mounted with DAPI (VECTASHIELD with DAPI, Vector Laboratories, Newark, California, USA) and stored in the dark at 4°C. Slides were imaged at 20× and 63× using a DM4 B microscopy system (Leica Biosystems, Wetzlar, Germany) with an LED 3 light source and a Cy5 filter set at 4×, 20×, and 63× magnifications. Image immunofluorescence intensity quantitation was determined for each of the four primary mouse lung lobes ($N = 4$ mice/lobe). A minimum of five images per lobe per animal were used in the analysis. All tissue images were analyzed using ImageJ software (Schneider et al. 2012).

Plasma Concentrations: Human Tf concentrations were determined in murine plasma after aerosol and subcutaneous dosing at 1, 2, 4, 8, 10 and 24 h using a commercial ELISA kit (human Tf, ab108911, Abcam).

3 | Results and Discussion

3.1 | Anion Exchange Chromatography Purification and SDS-PAGE Analysis

A protein cocktail bracketed between (50–100 kDa) was purified from Cohn fraction IV via TFF as described in the literature (Pires et al. 2021). A single-step anion exchange purification process was then used to purify Tf starting from the protein cocktail (Figure 1). Small-scale Tf purifications were first performed using 1 mL HiTrap columns with both strong and weak anion exchange resins, followed by 5 mL HiTrap Q FF columns (data not shown) to determine the optimal resin as well as protein binding and elution conditions. After optimization on small-scale columns, the purification process was scaled up to a 20 mL HiPrep Q FF column. A wash step of five CVs using 0% buffer B at 1 mL/min was applied to remove any unbound protein from the column. At 50 mM NaCl (10% buffer B), a

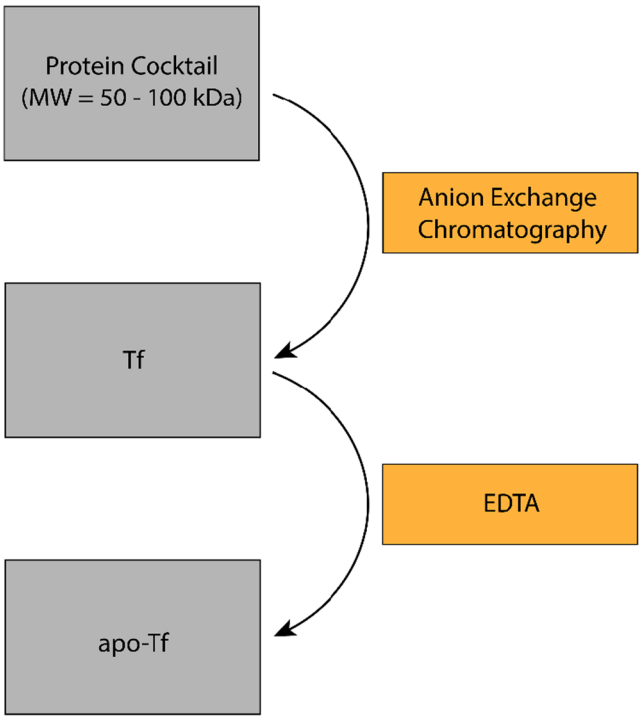

FIGURE 1 | Process flow diagram of the Tf purification process. The protein cocktail (50–100 kDa) derived from Cohn fraction IV was applied onto a HiPrep Q FF 16/10 column to remove contaminant proteins. The final purified Tf was then treated with EDTA while stirring at 4°C overnight to yield apo-Tf.

single peak was observed (peak 1, Figure 2A), made up primarily of human serum albumin (HSA), along with other proteins (Figure 2B). The second peak contained primarily Tf (peak 2, Figure 2A, and Figure 2B). The third peak contained primarily HSA and most of the non-Tf proteins (wash peak, Figure 2A, and Figure 2B). The major impurity remaining in the Tf rich fractions appears to be ~60 kDa in MW on the SDS-PAGE (Figure 2B) and could either be HSA or hemopexin (Hpx). Post purification, EDTA was used to remove Tf bound iron to obtain apo-Tf.

3.2 | MALDI-TOF Analysis

The protein cocktail (starting material) and purified apo-Tf were subjected to MALDI-TOF mass analysis (Figure 3). Mass spectral analysis of the protein cocktail shows that it contains a mixture of several expected proteins and consists primarily of human serum albumin (HSA), Tf, and hemopexin (Hpx) (Figure 3A). In the case of mass spectral analysis of the purified Tf, only a single major peak corresponding to the apparent molecular mass of Tf was observed (Figure 3B). A faint band at ~60 kDa was observed in the SDS-PAGE gel (Figure 2B), which appears to be hemopexin. However, MALDI mass spectrometry analysis did not detect hemopexin, but this could be attributed to differences in protein ionization (Hortin and Remaley 2006). The purified Tf molecular mass was determined to be 78.4 kDa (Figure 3B). The small difference between our measured value and previously reported Tf values can be attributed to variances in protein glycosylation (de Jong et al. 1990). The final product appeared free of contamination from other proteins when

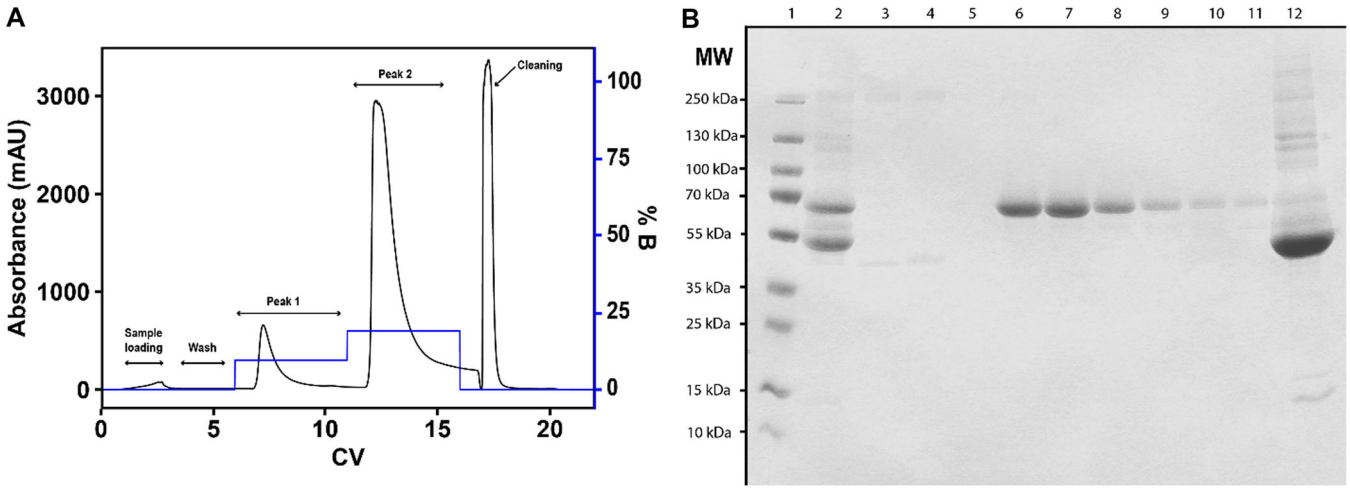

FIGURE 2 | Anion exchange chromatography of the protein cocktail derived from Cohn fraction IV to yield purified Tf. (A) Represents a typical chromatogram. The diluted protein cocktail was loaded onto a 20 mL HiPrep Q FF column. %B represents the amount of buffer B used to elute bound proteins. CV represents column volume. A wash was performed at 10% buffer B to remove contaminant proteins. The absorbance was monitored at 280 nm. (B) Represents a typical SDS-PAGE of the Q FF purification of Tf from the diluted protein cocktail. Lane 1: MW ladder. Lane 2: Protein cocktail. Lanes 3–5: Represent peak 1 fractions from Figure 2A. Lanes 6–11: Represent peak 2 fractions. Lane 12: Consists of a 2 M NaCl cleaning wash.

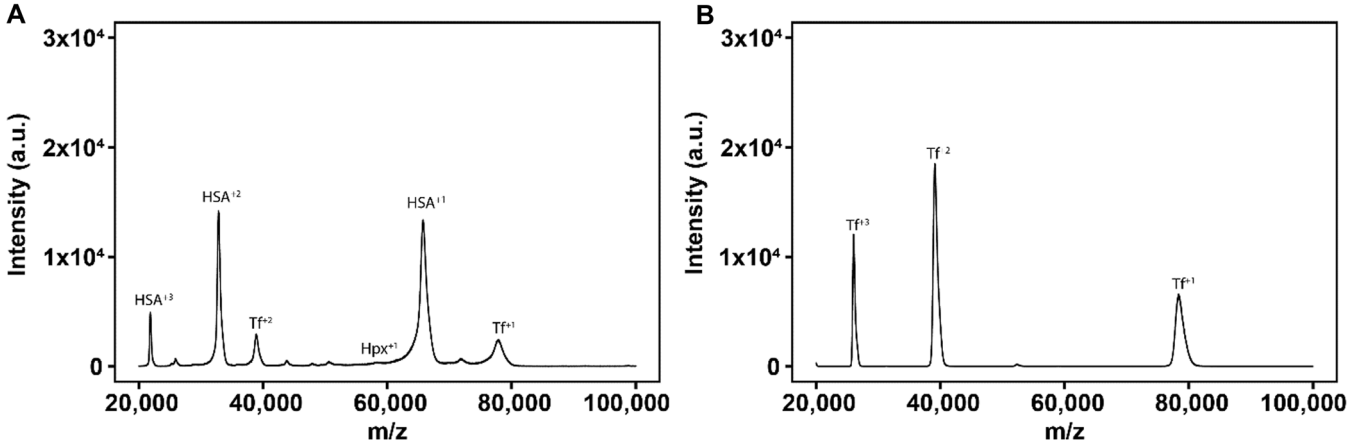

FIGURE 3 | MALDI-TOF analysis of the protein cocktail and purified Tf. (A) Represents a typical MALDI-TOF spectra of the protein cocktail, which was used as the starting material for the purification of Tf. The protein cocktail primarily consists of HSA with a MW of 66.5 kDa and Tf with a MW of 78.4 kDa. (B) Represents a typical MALDI-TOF spectra of the purified Tf product with a MW of 78.4 kDa.

comparing the final Tf product with the initial protein composition of the protein cocktail shown in Figure 3A. The protein cocktail is made up of HSA, Tf, and other plasma proteins and Figure 3A also shows the original protein cocktail, which has an intense signal at ~ 65 kDa, indicating the presence of HSA. The Tf peak is present at ~79 kDa but occurs at a much lower intensity in the protein cocktail.

3.3 | Trypsin Digest LC-MS/MS Analysis

Protein purity was first determined using a gel densitometric technique (Figure 2B) followed by trypsin digestion mass spectrometry for protein composition, and MW was confirmed using MALDI mass spectrometry (Figure 4). Tf purity was determined to be ~97% ± 1.5% from gel densitometry. However, trypsin digestion mass spectroscopy indicated that the purity of the final Tf product was closer to 95% ± 0.5% (Figure 4B). Although the Tf purity from densitometry is similar to what Von Bonsdorff et al. (2001) obtained in the past at 98%, the true purity we report is lower based on the accuracy of trypsin digestion mass spectrometry. Trypsin digestion mass spectroscopy was also performed on the protein cocktail starting material to obtain the initial composition of Tf in the protein cocktail. The total Tf yield was determined by comparing the final mass of purified Tf against the initial mass of Tf in the protein cocktail (Table 1). A significant amount of Tf may have been lost in the fractions that contained significant impurities. Additionally, some Tf was lost in the 10% buffer B wash step or remained bound to the column until the 2 M NaCl wash step, and this likely decreased the overall Tf yield.

3.4 | UV-Visible Spectroscopy

The activity of the purified Tf was assessed using UV-visible spectroscopy (Figure 5). Apo- and holo-Tf have an identical absorption band at ~280 nm, which is attributed to the aromatic

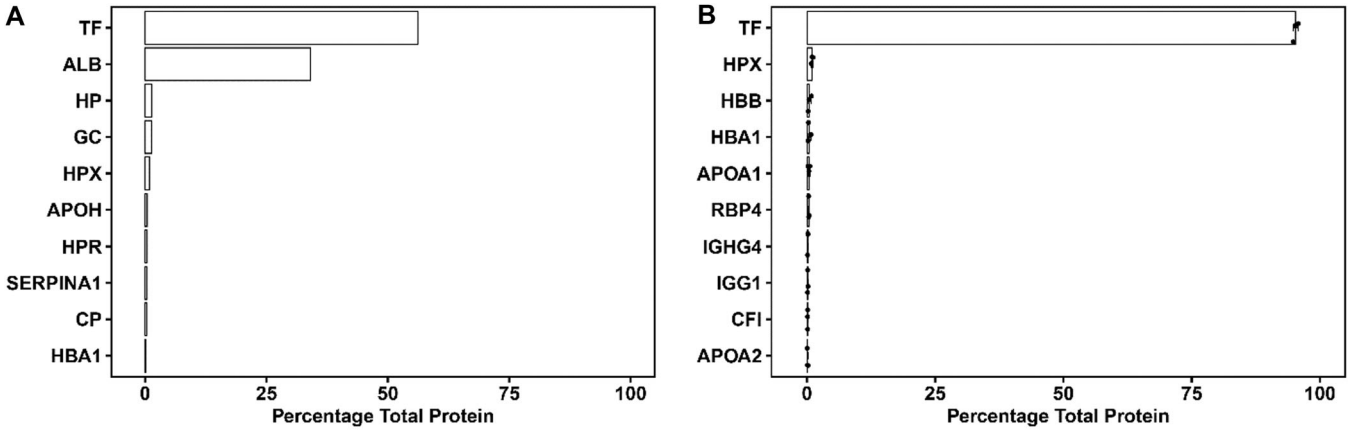

FIGURE 4 | Trypsin digest mass spectrometry analysis of the protein cocktail and purified Tf. Both figures show the ten most abundant proteins and cover > 99% of all proteins in the sample. (A) Represents the protein composition of the protein cocktail that was used as the starting material for the purification of Tf. The error bars were derived from three separate purifications. (B) Represents the protein composition of the purified Tf. The error bars were derived from three separate purifications. Abbreviations: ALB, albumin; APOA1, apolipoprotein A-I; APOA2, apolipoprotein A-II; APOH, beta-2-glycoprotein; CFI, complement factor I; CP, ceruloplasmin; GC, vitamin D-binding protein; HBA1, hemoglobin subunit alpha; HBB, hemoglobin subunit beta; HP, haptoglobin; HPR, haptoglobin related protein; HPX, hemopexin; IGG1, immunoglobulin gamma-1 heavy chain; IGHG4, immunoglobulin heavy constant gamma 4; RBP4, retinol-binding protein 4; SERPINA1, alpha-1-antitrypsin; TF, transferrin.

TABLE 1 | Estimation of Tf purity and yield.

Starting material (i.e., protein cocktail)	Purified material		
Tf mass (mg)	Tf mass (mg)	Tf purity (%)	Yield (%)
2030.1 ± 90.3	1074.4 ± 124.2	95.3 ± 0.48	52.9

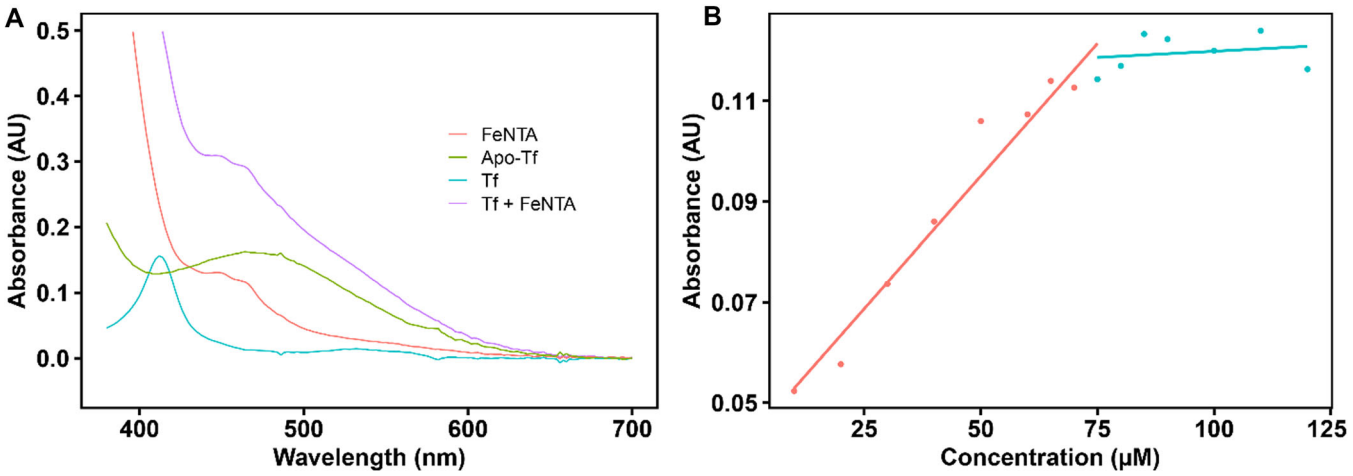

FIGURE 5 | (A) Ferric Fe binding capacity of purified apo-Tf. Purified Tf and FeNTA were incubated together for 2 h at 25°C and the absorbance spectra was measured using UV-visible spectrometry. The spectra of FeNTA, Tf, and Tf + FeNTA were experimentally measured, and the apo-Tf spectra were calculated by subtracting the FeNTA and Tf spectra from the Tf + FeNTA spectra. The absorbance peak at 470 nm was used to determine the amount of iron bound to purified Tf. (B) Fe titration of purified Tf. Purified Tf and increasing concentrations of FeNTA were incubated for 1 h at 25°C. Samples were aliquoted into a 96-well plate at a volume of 350 μL. The absorbance was measured at 450 nm and fitted to 2 linear functions to determine the Fe saturation point of the purified Tf.

amino acid residues in the protein. However, Fe-bound Tf has a unique characteristic absorption band at ~470 nm due to metal-protein interactions, which is attributed to the phenomena of ligand to metal charge transfer (Byrne et al. 2010). This indicates that the purified protein is properly folded and has intact ligand- binding properties. We further used this characteristic Fe-specific absorption band of Tf for the quantification of protein activity. For this assay, apo-Tf was incubated with FeNTA for 2 h at room temperature. The difference in absorbance between Tf with bound ferric Fe, Tf by itself, and ferric Fe by itself was calculated to determine the total amount of holo-Tf produced in the reaction (Figure 5A). This relative increase was

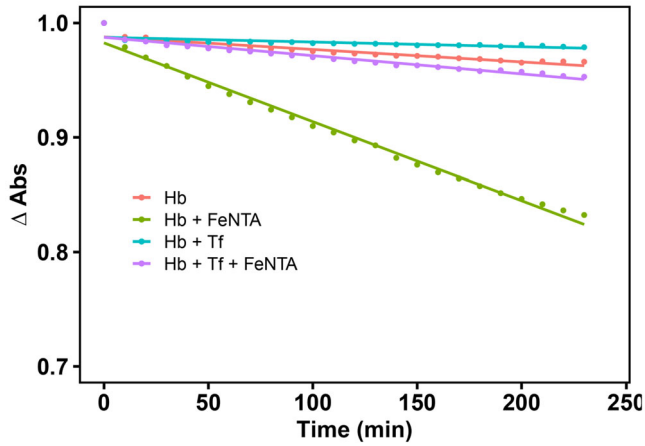

FIGURE 6 | Auto-oxidation of Hb in the presence or absence of free ferric Fe and Tf. Absorbance changes were measured over a 4 h time-frame at 25°C with a time point taken every 10 min.

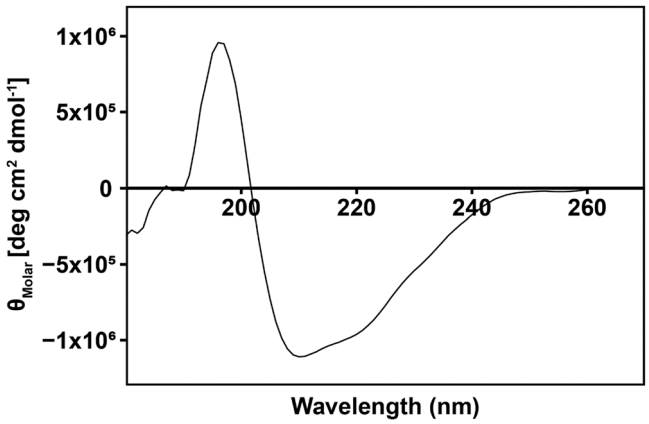

FIGURE 7 | Far UV CD spectra of apo-Tf in 50 mM PB, at pH 7.4.

used to determine the amount of active apo-Tf in the sample before incubation with FeNTA. From this study, we determined that the amount of active protein (i.e., apo-Tf) available to bind to ferric Fe was ~90.9 ± 14.8%. Titration of the purified Tf at a concentration of 36 μM was performed with increasing concentrations of FeNTA (Figure 5B). The saturation point was determined to be ~75 μM FeNTA, which very closely replicates the expected value for Tf at a protein: ligand binding ratio of 1:2 (Tf: Fe^{3+}) and provides additional evidence that the purified Tf is primarily in the apo-protein form.

Auto-oxidation of Hb occurs naturally when the environment surrounding Hb is devoid of antioxidants and generates superoxide, a reactive oxygen species (ROS) that can damage surrounding tissue (Winterbourn 1990). The auto-oxidation rate constant of Hb has been reported in the past as $4.5 \times 10^{-7}\,s^{-1}$ (Johnson et al. 2005), which is close to our experimental $k_{auto\text{-}ox}$ of $2 \times 10^{-6}\,s^{-1}$ under similar experimental conditions. However, Hb exhibits a higher auto-oxidation rate constant when exposed to free ferric Fe ($k_{auto\text{-}ox} = 1 \times 10^{-5}\,s^{-1}$), but this is attenuated by the addition of Tf ($k_{auto\text{-}ox} = 3 \times 10^{-6}\,s^{-1}$) (Figure 6). When only Tf is added to Hb, the auto-oxidation rate constant of Hb decreases to $7 \times 10^{-7}\,s^{-1}$. This shows that apo-Tf reduces auto-oxidation of Hb both in the presence and absence of free Fe, which is consistent with the literature (Baek et al. 2017).

3.5 | Circular Dichroism Spectroscopy

The secondary structure of purified apo-Tf, was analyzed by circular dichroism (CD) spectroscopy (Figure 7). Tf shows a single positive peak at ~196 nm, and a major negative peak at ~208 nm, followed by a minor negative peak at ~218 nm. This shows that the protein primarily consists of antiparallel β sheets with a relatively smaller amount of α helices. CD analysis shows that the protein is properly folded, and our results are in agreement with the literature (Tang et al. 1995).

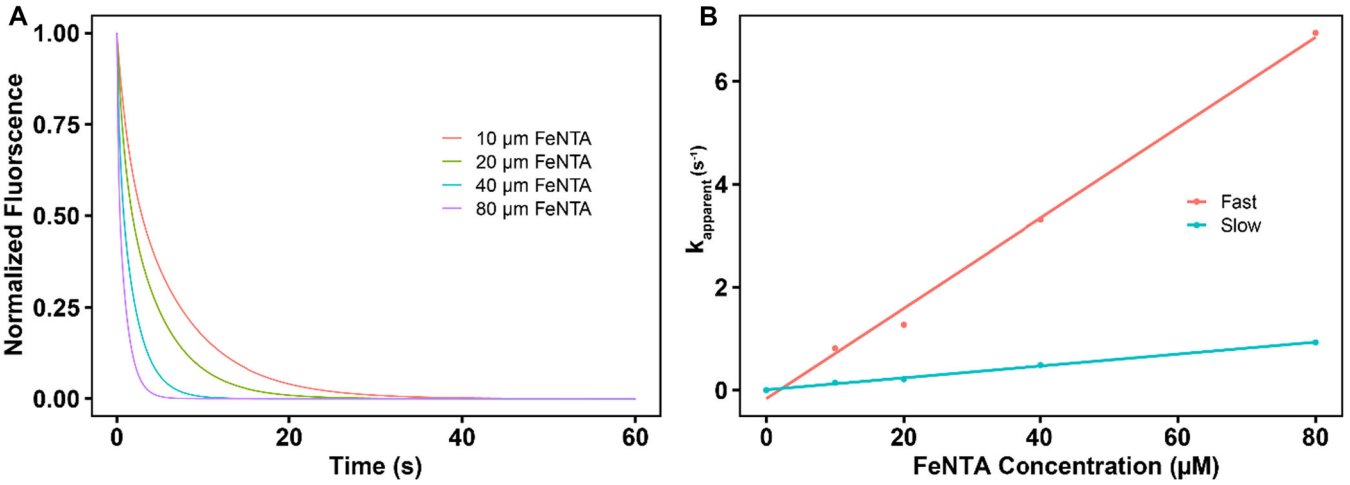

FIGURE 8 | Kinetics of Fe binding to Tf. (A) Stopped flow kinetic traces of fluorescence quenching obtained upon binding of 5 μM Tf with increasing concentrations of FeNTA from 10.0–80.0 μM. Each kinetic trace represents an average of 10 scans and were fit to a biexponential function to obtain $k_{apparent}$ (pseudo first-order rate constant). (B) Linear fit of $k_{apparent}$ as a function of Tf concentration for regression of the fast and slow second-order rate constants for the binding of FeNTA with apo-Tf.

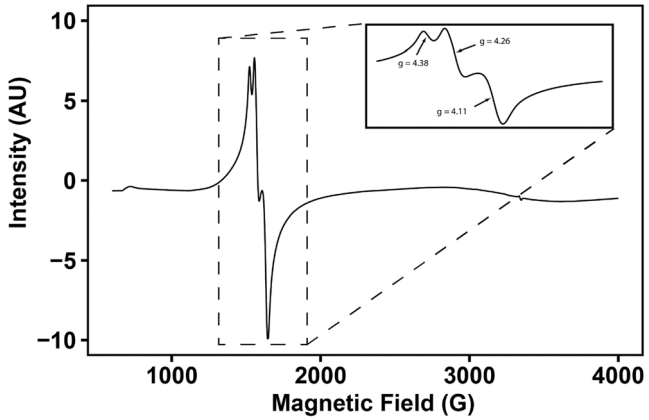

FIGURE 9 | EPR spectra of holo-Tf. Purified apo-Tf was incubated with FeNTA for 2 h at room temperature on a shaker at 100 rpm. EPR measurements were taken at 20 K on an X-Band (9.4 Ghz) EMXPlus with the center field at 2600 G and sweep width of 4000 G. The receiver gain was set at 30 dB, modulation amplitude at 10 G, microwave attenuation at 20 dB, and microwave power at 2 mW. Five measurements were averaged to increase the signal-to-noise ratio.

3.6 | Fe Binding Kinetics

The kinetics of Fe binding to Tf has been reported in the literature as a two-step process, in which ferric Fe bound to a chelator such as NTA binds to Tf, followed by the loss of NTA (Bates and Wernicke 1971).

$$\mathrm{Fe(III)-NTA+Tf \rightleftarrows Fe(III)-NTA-Tf \rightleftarrows Fe(III)-Tf+NTA}$$

The binding kinetics of Fe to Tf was monitored by measuring the fluorescence change at 285 nm on a stopped flow spectrophotometer (Figure 8A). The bimolecular rate constant was found by fitting the apparent rate constants as a linear function of FeNTA concentration and found to be $k_{\mathrm{fast}} = 1.9 \times 10^5\,\mathrm{M^{-1}s^{-1}}$, and $k_{\mathrm{slow}} = 3.0 \times 10^4\,\mathrm{M^{-1}s^{-1}}$ (Figure 8B). This compares to the rate constant Pakdaman and Chahine (1996) previously determined of $k = 8.0 \times 10^4$, but differs because our pseudo-first-order data was fit to a biexponential function. We believe the data is better explained by a fast and a slow rate, based on the reaction mechanism of FeNTA binding to Tf. The interaction between

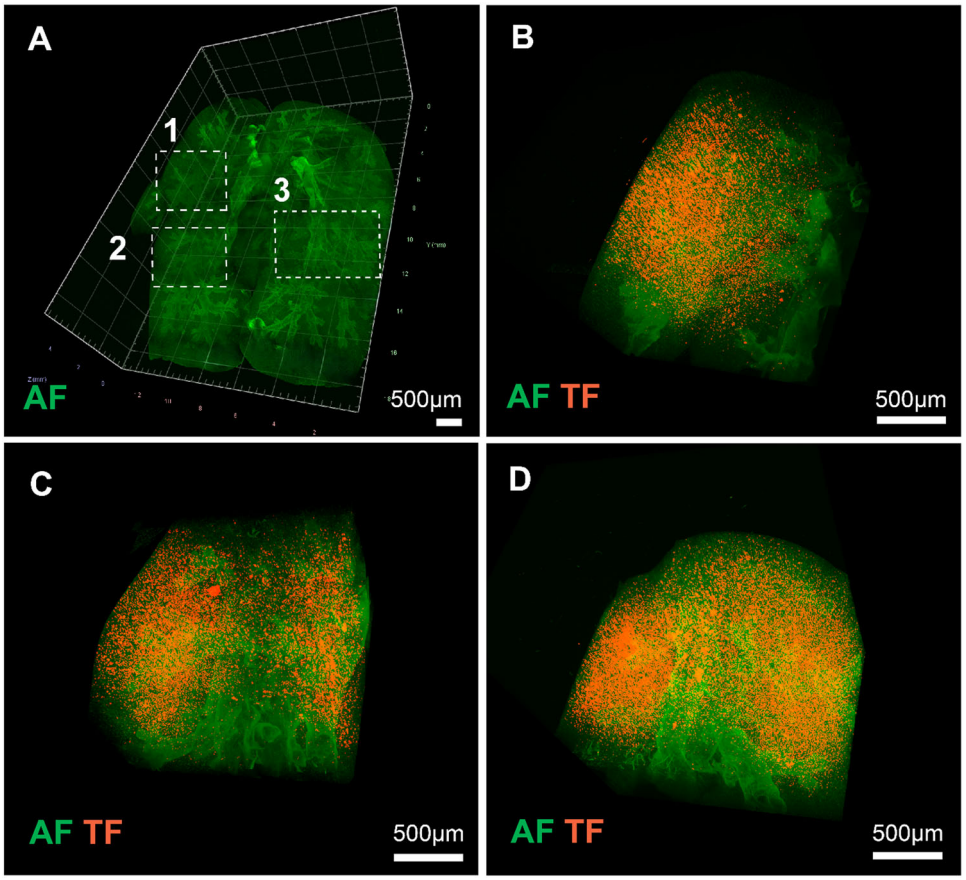

FIGURE 10 | Qualitative 3D reconstruction of whole lung using light sheet microscopy of Tf distribution. (A) Light sheet microscopy of Berk-SS mouse whole lung showing autofluorescence (AF, in green) after laser excitation at 488 nm. (B) Shows a section of the right superior lung lobe (Box 1) to highlight the distribution of Alexa fluor 647 conjugated Tf fluorescence after laser excitation at 638 nm (red) merged with autofluorescence. (C) Shows the right middle lung lobe (Box 2) with Alexa fluor 647 conjugated Tf fluorescence merged with autofluorescence. (D) Shows the left lung lobe (Box 3) with Alexa fluor 647 conjugated Tf fluorescence merged with autofluorescence. A movie for (A–D) is provided in the Supporting Information. All images were captured using a 5× detection objective, and each illumination collar is set at 1.52 to match the refractive index of the Cubic solutions. All scale bars = 500 µm.

FeNTA and Tf is described by the fast rate, where the Fe binds to Tf, while the slow rate captures stabilization of the Fe atom by a carbonate anion and removal of the NTA moiety.

3.7 | EPR Spectroscopy

Post incubation with FeNTA, Tf was characterized for its ability to bind to Fe via EPR spectroscopy at 20K and yielded three distinct peaks (Figure 9). The *g*-factor was assigned to the inflection point between a peak and a trough for a region with the highest amplitude and was used to characterize the magnetic moment and angular momentum of the Fe atom bound to Tf. The *g*-factors for Tf coordinated ferric Fe measured in the past are, in order of increasing magnetic induction, g ~ 4.36–4.39, g~ 4.19–4.25, g~4.07–4.12 (Kubiak et al. 2013; Rottman et al. 1989). In that study, the Fe iron was present in a high-spin state of $S = 5/2$ and is bound in a distorted octahedral coordination with four amino acids and two oxygen atoms from the carbonate ion to synergistically bind Fe^{3+} to Tf (Adams et al. 2003; Faber et al. 1996). Although carbonate ions have been used in the past for EPR studies on Fe-bound Tf (i.e., holo-Tf), our present EPR study did not have experimentally added carbonate ions, but still exhibited the same coordination for Fe with *g*-factors of $g = 4.38$, $g = 4.26$, and $g = 4.11$ with increasing magnetic induction (Figure 9). This suggests ferric Fe is in the correct coordination state, and bicarbonate ions were found in solution under ambient conditions during sample preparation upon exposure to the atmosphere, which contains carbon dioxide (Bates and Wernicke 1971).

In summary, the approach to purification and characterization of apo-Tf suggested a highly pure and efficient iron binding protein that could be useful in diseases where reactive iron contributes toward pathophysiology. Targeting lung regions that have iron accumulation, such as that observed in SCD pulmonary hypertension offer a novel use for Tf using intrapulmonary lung delivery.

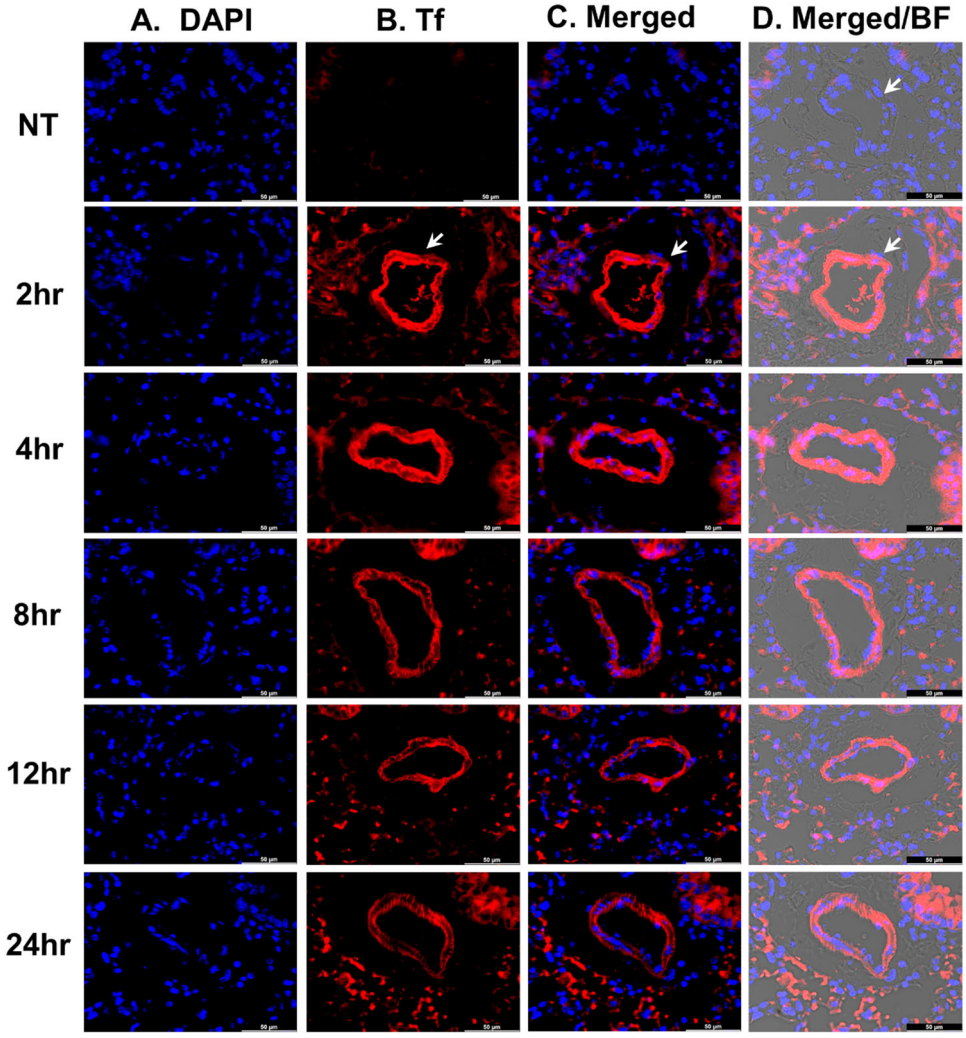

FIGURE 11 | Time course of lung vascular Tf distribution after intrapulmonary dosing. Representative images of tissue sections prepared from the left lung lobe are shown for nontreated (NT–Not treated), 2, 4, 8, 12, and 24 h after intrapulmonary dosing. (A) Shows DAPI (4′,6-diamidino-2-phenylindole) nuclear staining (Blue). (B) Shows Tf immunofluorescence in and around blood vessels (Red). (C) Shows the merged image of DAPI with Tf. (D) Shows the brightfield merge to allow for visualization of structural features. Lung vascular smooth muscle tissue images were obtained at 63× objective magnification, scale bars = 50 μm. Arrows indicate the location of blood vessels.

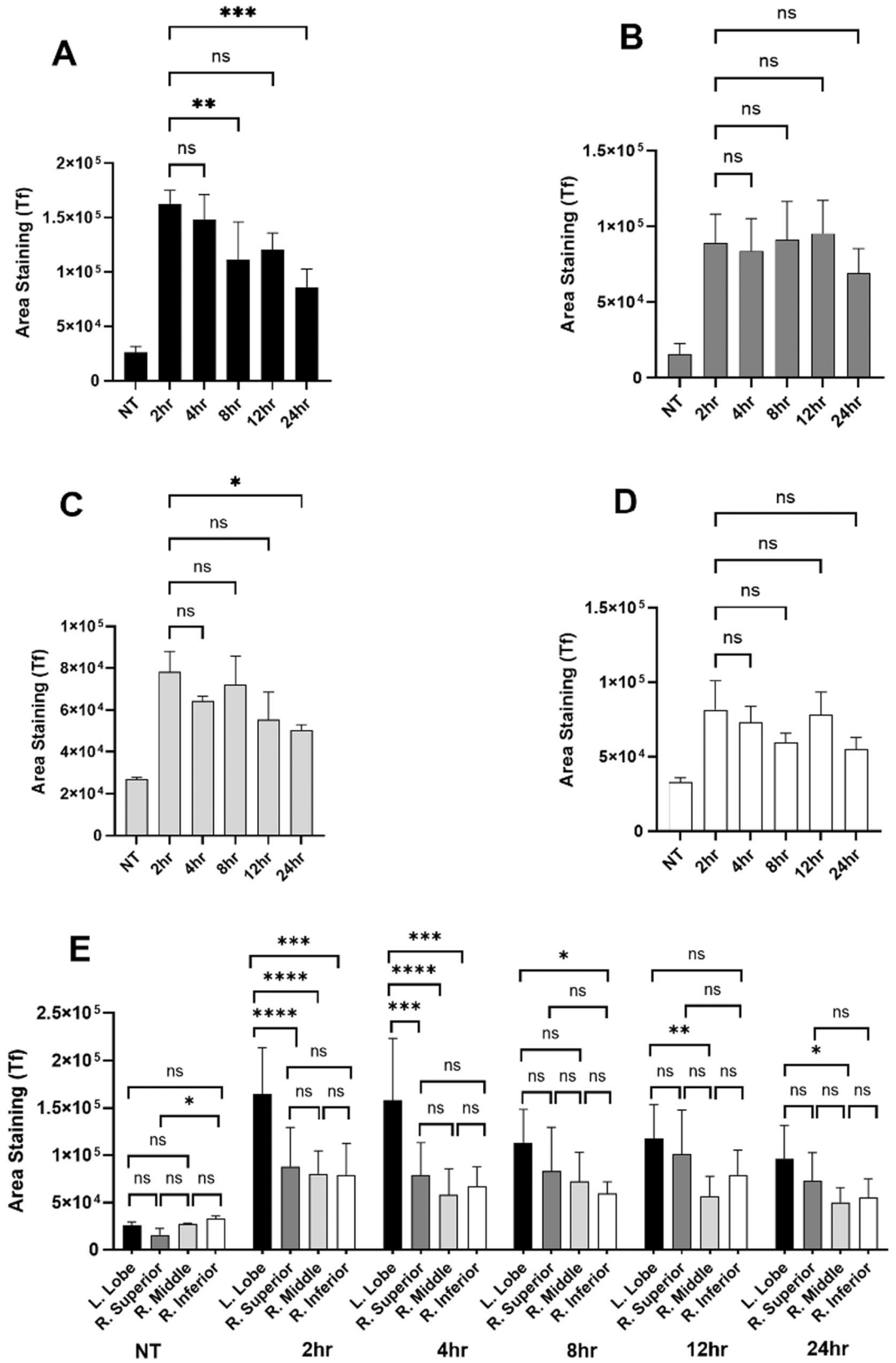

FIGURE 12 | Tf distribution to murine lung lobes after intra-pulmonary dosing. (A–D) shows the mean fluorescence intensity for Tf derived immunofluorescence staining area for the left, right superior, right middle, and right inferior lung lobes, respectively. (E) Shows the mean fluorescence intensity for Tf comparing fluorescence intensity between lung lobes over 24 h post-dosing. Image immunofluorescence intensity quantitation was determined for each of the four primary mouse lung lobes ($N = 4$ mice/lobe). A minimum of five images per lobe per animal were used in the analysis. All tissue images were analyzed using ImageJ software (Schneider et al. 2012). Data shown as mean ± SD, significance in this data set are shown as $^{*}p < 0.05$, $^{**}p < 0.01$, $^{***}p < 0.001$, $^{****}p < 0.0001$.

3.8 | Whole Lung Distribution of Tf in Berk-SS Mice

Hemolytic severity is associated with increased pulmonary systolic pressure and is a risk factor for death in SCD (Nouraie et al. 2013). Data from humans and murine models supports that hemoglobin (Hb) and its degradation product, heme are important toxins that drive vasculopathy in SCD (Reiter et al. 2002; Belcher et al. 2014). Macrophages with iron accumulation are present in the lung vasculature of humans and murine models of pulmonary hypertension (Redinus et al. 2019; Ferguson et al. 2019). The cell type is consistent with macrophages that accumulate in the vascular adventitia and export iron into the localized tissue environment (Buehler et al. 2021). Based on this finding, we tested if the human apo-Tf preparation could be delivered to the distal lung in Berk-SS mice following aerosolized intra-pulmonary administration. Light sheet microscopy of lungs excised from Berk-SS mice after dosing with Alexa Fluor 647 conjugated to purified human apo-Tf are shown in Figure 10. Autofluorescence (AF) is shown in green after laser excitation at 488 nm (Figure 10A). A section of the right superior lung lobe (box 1 region, Figure 10A) shows distribution of Alexa fluor 647 conjugated Tf fluorescence after laser excitation at 638 nm (red) merged with autofluorescence (Figure 10B). Images merging AF and Alexa fluor 647 conjugated Tf fluorescence for the right middle lobe (box 2, Figure 10A) is shown in Figure 10C. Images merging AF and Alexa fluor 647 conjugated Tf fluorescence for the left lobe (box 3, Figure 10A) is shown in Figure 10D. The right superior and middle lobe sections as well as the left lobe section are provided in the Supporting Information S1–S3: Movies 1–3. Typically, particles $< 1\,\mu m$ distribute to distal airways, while particles $> 1\,\mu m$ deposit in the bronchi and bronchioles (collectively known as conducting airways). The present data shows our delivery method that aerosolizes particles indeed distributes them to the distal lung sites that are downstream of conducting airways.

3.9 | Lung Vascular Accumulation of Tf After Intra-Pulmonary Dosing

We next sought to determine if the distribution of intra-pulmonary aerosolized apo-Tf could be localized in the lung vasculature, which is the specific anatomical region of interest for delivery. In Berk-SS mice, intrapulmonary dosing of Tf shows localization to the lung vasculature (Figure 11). Here, the left lobe is shown as a representative for vascular tissue accumulation. Nonetheless, the distribution of Tf throughout the lung shows immunofluorescence of Tf protein in all major lung lobes (Figure 12). The major lobes of the left lung show Tf protein fluorescence intensity at 2, 4, 8, 12 and 24 h after intrapulmonary dosing (Figure 12A). The major lobes of the right lung include the superior, middle, and inferior lobes and each show accumulation of protein at 2, 4, 8, 12 and 24 h after intrapulmonary dosing (Figure 12B–D). Except for the left lobe at 2 and 4 h post administration, all lobes demonstrated similar retention of Tf after its intrapulmonary administration. The mean fluorescence intensity for Tf comparing fluorescence intensity between lung lobes over 24 h post-dosing is shown in Figure 12E, indicating the left lobe receives a significantly greater distribution of Tf compared to the right lung lobes.

It is worth noting that the anti-Tf antibody used in Figure 11 does have cross reactivity with murine and human Tf. Therefore, the absence of a signal from the NT mice reflects the comparatively low concentration of endogenous Tf in the lung vasculature compared with the human Tf dosed mice.

Tf plasma concentrations were determined to understand if the dosed protein was retained in the lungs or if pulmonary vascular absorption led to accumulation of Tf in the systemic circulation. Plasma concentration versus time data was compared after subcutaneous and intra-pulmonary injection (Figure 13). Subcutaneous injection (300 mg/kg) of Tf for 5 days resulted in a steady state plasma concentration of 0.35 ± 0.022 mg/mL and

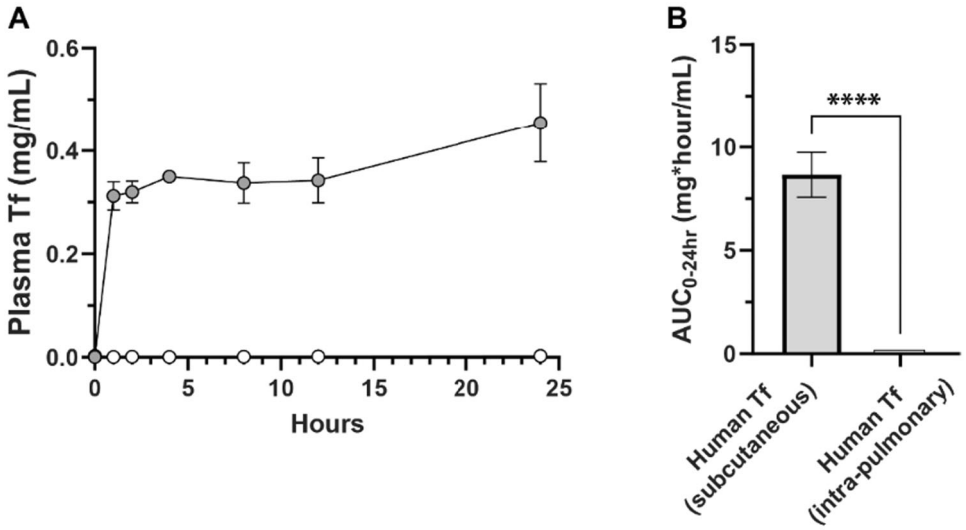

FIGURE 13 | Tf plasma concentrations. (A) Shows the plasma concentrations of human plasma-derived Tf after intra-pulmonary dosing (open circles) and subcutaneous dosing (grey circles). Time points were before dosing (0 h), 1, 2, 4, 8, 12 and 24 h after dosing ($N = 4$ mice per time point). (B) Shows the AUC values for subcutaneous dosing and intra-pulmonary dosing AUC values were calculated using the linear trapezoidal rule from time 0–24 h. Data are shown as the mean ± SD, significance in this data set are shown as ****$p < 0.0001$.

an area under the plasma concentration time curve (AUC) of 8.66 ± 1.10 mg*h/mL in Berk-SS mice. After intra-pulmonary Tf injection (300 mg/kg) plasma concentrations did not exceed 3 μg/mL (approximately 100 times lower than subcutaneous injection) over a 24-h period after the last administration. Based on our calculation pulmonary bioavailability (%F) using the formula $(\%F = \text{AUC}_{\text{intra-pulmonary}}/\text{AUC}_{\text{subcutaneous}}) \times 100$, less than 1% of Tf administered to lung was detectable in the plasma. These data suggest that intra-pulmonary delivery of Tf would have only localized effects at the lung vasculature, which may be effective for further evaluation in SCD pulmonary hypertension mouse models.

4 | Conclusion

Our observations of lung vascular pathology in SCD patients with PH shows a clear iron and oxidative role within the lung vasculature (Buehler et al. 2021; Redinus et al. 2019). This observation is unique and not observed in idiopathic PH or in SCD patients without PH (Buehler et al. 2021). Therefore, we developed the current study to purify apo-Tf from Cohn fraction IV paste using a scalable process with a priori knowledge of pulmonary vascular iron deposition in SCD PH. Further, this study for the first time demonstrates potential for the use of an aerosolized large protein (~80 kDa) that directly reaches the peripheral lung and sites of pathology. We expect that this purification process will allow for apo-Tf production at a scale needed for preclinical proof-of-concept effectiveness studies. Indeed, aerosol intra-pulmonary therapeutic delivery may prevent the need for intravenous or subcutaneous administration of novel therapeutic proteins. Translational aspects of this study offer insight into a disease specific application (i.e., SCD PH), which currently has no options for treatment and significantly increases morbidity and mortality (Gordeuk et al. 2016).

Author Contributions

All authors, S.L., M.A.K, S.S., Q.O., K.T., P.C., D.C.S, D.C.I., P.W.B, and A.F.P., were involved in the conceptualization, experimental design, data curation, and formal analysis of the study. S.L., M.A.K., and Q.O. contributed to the purification and characterization of the material. P.W.B., K.T., and S.S. contributed to the in vivo analysis of the material. The initial draft of the manuscript was prepared by S.L., M.A.K, Q.O., P.W.B., and A.F.P. Additionally, all authors (S.L., M.A.K, S.S., Q.O., K.T., P.C., D.C.S, D.C.I., P.W.B, and A.F.P.) were responsible for manuscript revision, editing, and finalization for publication. Funding acquisition was managed by A.F.P., P.W.B., D.C.I, and P.C.

Acknowledgments

This study was supported by the National Institutes of Health under grants R01HL158076, R01HL159862, and R01HL162120; as well as, the US Army Medical Research Acquisition Activity under the Congressionally Directed Medical Research Programs Focused Program Award HT94252410238 to A.F.P., P.W.B, P.C., and D.C.I. We acknowledge resources from the Campus Chemical Instrumentation Center Mass Spectrometry and Proteomics Facility and the Ohio State University (OSU) Comprehensive Cancer Center (OSUCCC) Proteomics Shared Resource (PSR), The Ohio State University. This facility is supported in part by funding from OSU's Enterprise for Research, Innovation and Knowledge and NCI grant P30 CA016058. We acknowledge the University of Maryland School of Medicine CIBR Confocal Microscopy core for access to light sheet microscopy imaging technology. Opinions, interpretations, conclusions, and recommendations are those of the authors and are not necessarily endorsed by the National Institutes of Health and the US Department of Defense.

Disclosure

A.F.P. and S.L. are co-inventors on a US provisional patent application related to this study.

Data Availability Statement

The data that supports the findings of this study are available in the supporting material of this article.

References

Adams, T. E., A. B. Mason, Q. Y. He, et al. 2003. "The Position of Arginine 124 Controls the Rate of Iron Release From the N-Lobe of Human Serum Transferrin." *Journal of Biological Chemistry* 278: 6027–6033.

Ali, M. K., R. Y. Kim, A. C. Brown, et al. 2020. "Critical Role for Iron Accumulation in the Pathogenesis of Fibrotic Lung Disease." *Journal of Pathology* 251: 49–62.

Anderson, B. F., H. M. Baker, G. E. Norris, D. W. Rice, and E. N. Baker. 1989. "Structure of Human Lactoferrin: Crystallographic Structure Analysis and Refinement at 2·8 Å Resolution." *Journal of Molecular Biology* 209: 711–734.

Ascione, E., L. Muscariello, V. Maiello, et al. 2010. "A Simple Method for Large-Scale Purification of Plasma-Derived Apo-Transferrin." *Biotechnology and Applied Biochemistry* 57: 87–95.

Bacon, B. R., G. M. Brittenham, A. S. Tavill, C. E. McLaren, C. H. Park, and R. O. Recknagel. 1983. "Hepatic Lipid Peroxidation In Vivo in Rats With Chronic Dietary Iron Overload Is Dependent on Hepatic Iron Concentration." *Transactions of the Association of American Physicians* 96: 146–154.

Baek, J. H., A. Yalamanoglu, Y. Gao, et al. 2017. "Iron Accelerates Hemoglobin Oxidation Increasing Mortality in Vascular Diseased Guinea Pigs Following Transfusion of Stored Blood." *JCI Insight* 2: 1–14.

Bates, G. W., and J. Wernicke. 1971. "The Kinetics and Mechanism of Iron (III) Exchange Between Chelates and Transferrin." *Journal of Biological Chemistry* 246: 3679–3685.

Belcher, J. D., C. Chen, J. Nguyen, et al. 2014. "Heme Triggers TLR4 Signaling Leading to Endothelial Cell Activation and Vaso-Occlusion in Murine Sickle Cell Disease." *Blood* 123: 377–390.

Bradford, M. M. 1976. "A Rapid and Sensitive Method for the Quantitation of Microgram Quantities of Protein Utilizing the Principle of Protein-Dye Binding." *Analytical Biochemistry* 72: 248–254.

Britton, R. S., G. A. Ramm, J. Olynyk, R. Singh, R. O'Neill, and B. R. Bacon. 1994. "Pathophysiology of Iron Toxicity." *Advances in Experimental Medicine and Biology* 356: 239–253.

Buehler, P. W., D. Swindle, D. I. Pak, et al. 2021. "Hemopexin Dosing Improves Cardiopulmonary Dysfunction in Murine Sickle Cell Disease." *Free Radical Biology and Medicine* 175: 95–107.

Byrne, S. L., N. D. Chasteen, A. N. Steere, and A. B. Mason. 2010. "The Unique Kinetics of Iron Release From Transferrin: The Role of Receptor, Lobe-Lobe Interactions, and Salt at Endosomal pH." *Journal of Molecular Biology* 396: 130–140.

Cancado, R. D., M. C. A. Olivato, N. N. L. Filho, O. Campos, and C. Chiattone. 2008. "Pulmonary Hypertension as a Risk Factor for Death in Patients With Sickle Cell Anemia." *Blood* 112: 4819.

Cohn, E. J., L. E. Strong, W. L. Hughes, et al. 1946. "Preparation and Properties of Serum and Plasma Proteins. IV. A System for the Separation Into Fractions of the Protein and Lipoprotein Components of

Biological Tissues and Fluids." *Journal of the American Chemical Society* 68: 459–475.

Elsayed, M. E., M. U. Sharif, and A. G. Stack. 2016. *Transferrin Saturation: A Body Iron Biomarker. Advances in Clinical Chemistry. Vol. 75*. Elsevier Inc.

Faber, H. R., C. J. Baker, C. L. Day, J. W. Tweedie, and E. N. Baker. 1996. "Mutation of Arginine 121 in Lactoferrin Destabilizes Iron Binding by Disruption of Anion Binding: Crystal Structures of R121S and R121E Mutants." *Biochemistry* 35: 14473–14479.

Ferguson, S. K., K. Redinius, A. Yalamanoglu, et al. 2019. "Effects of Living at Moderate Altitude on Pulmonary Vascular Function and Exercise Capacity in Mice With Sickle Cell Anaemia." *Journal of Physiology* 597: 1073–1085.

Frieden, E., and P. Aisen. 1980. "Forms of Iron Transferrin." *Trends in Biochemical Sciences* 5: xi.

Gelderman, M. P., J. H. Baek, A. Yalamanoglu, et al. 2015. "Reversal of Hemochromatosis by Apotransferrin in Non-Transfused and Transfused Hbbth3/+ (Heterozygous b1/b2 Globin Gene Deletion) Mice." *Haematologica* 100: 611–622.

Ginzburg, Y., X. An, S. Rivella, and A. Goldfarb. 2023. "Normal and Dysregulated Crosstalk Between Iron Metabolism and Erythropoiesis." *eLife* 12: 1–37.

Gordeuk, V. R., O. L. Castro, and R. F. Machado. 2016. "Pathophysiology and Treatment of Pulmonary Hypertension in Sickle Cell Disease." *Blood* 127: 820–828.

Hentze, M. W., M. U. Muckenthaler, and N. C. Andrews. 2004. "Balancing Acts: Molecular Control of Mammalian Iron Metabolism." *Cell* 117: 285–297.

Hortin, G. L., and A. T. Remaley. 2006. "Mass Determination of Major Plasma Proteins by Matrix-Assisted Laser Desorption/Ionization Time-of-Flight Mass Spectrometry." *Clinical Proteomics* 2: 103–115.

Howard, J., C. J. Hemmaway, P. Telfer, et al. 2019. "A Phase 1/2 Ascending Dose Study and Open-Label Extension Study of Voxelotor in Patients With Sickle Cell Disease." *Blood* 133: 1865–1875.

Inman, J. K., F. C. Coryell, K. B. McCall, et al. 1961. "A Large-Scale Method for the Purification of Human Transferrin." *Vox Sanguinis* 6: 34–52.

Ishihama, Y., Y. Oda, T. Tabata, et al. 2005. "Exponentially Modified Protein Abundance Index (emPAI) for Estimation of Absolute Protein Amount in Proteomics by the Number of Sequenced Peptides Per Protein." *Molecular & Cellular Proteomics* 4: 1265–1272.

Jackson, S., and B. C. Morris. 1961. "Enhancement of Growth of Pasteurella Pestis and Other Bacteria in Serum by the Addition of Iron." *British Journal of Experimental Pathology* 42: 363–368.

Johnson, R., G. Goyette Jr., Y. Ravindranath, and Y. Ho. 2005. "Hemoglobin Autoxidation and Regulation of Endogenous H_2O_2 Levels in Erythrocytes." *Free Radical Biology and Medicine* 39: 1407–1417.

de Jong, G., J. P. van Dijk, and H. G. van Eijk. 1990. "The Biology of Transferrin." *Clinica Chimica Acta* 190: 1–46.

Kistler, P., H. Nitschmann, A. Wyttenbach, M. Studer, C. Niederöst, and M. Mauerhofer. 1960. "Humanes Siderophilin: Isolierung Mittels Rivanol Aus Blutplasma Und Plasmafraktionen, Analytische Bestimmung Und Kristallisation." *Vox Sanguinis* 5: 403–415.

Koechlin, B. A. 1952. "Preparation and Properties of Serum and Plasma Proteins. XXVIII. The β1-Metal-Combining Protein of Human Plasma." *Journal of the American Chemical Society* 74: 2649–2653.

Kubiak, T., R. Krzyminiewski, and B. Dobosz. 2013. "EPR Study of Paramagnetic Centers in Human Blood." *Current Topics in Biophysics* 36: 7–13.

Lamb, D. R., A. Greenfield, K. Thangaraju, et al. 2023. "The Molecular Size of Bioengineered Oxygen Carriers Determines Tissue Oxygenation in a Hypercholesterolemia Guinea Pig Model of Hemorrhagic Shock and Resuscitation." *Molecular Pharmaceutics* 20: 5739–5752.

Leibman, A. J., and P. Aisen. 1967. "Preparation of Single Crystals of Transferrin." *Archives of Biochemistry and Biophysics* 121: 717–719.

MacGillivray, R. T., E. Mendez, J. G. Shewale, S. K. Sinha, J. Lineback-Zins, and K. Brew. 1983. "The Primary Structure of Human Serum Transferrin. The Structures of Seven Cyanogen Bromide Fragments and the Assembly of the Complete Structure." *Journal of Biological Chemistry* 258: 3543–3553.

McCann, K. B., B. Hughes, J. Wu, J. Bertolini, and P. T. Gomme. 2005. "Purification of Transferrin From Cohn Supernatant I Using Ion-Exchange Chromatography." *Biotechnology and Applied Biochemistry* 42: 211–217.

Misra, H., J. Bainbridge, J. Berryman, et al. 2017. "A Phase Ib Open Label, Randomized, Safety Study of SANGUINATE™ in Patients With Sickle Cell Anemia." *Revista Brasileira de Hematologia e Hemoterapia* 39: 20–27.

Nouraie, M., J. S. Lee, Y. Zhang, et al. 2013. "The Relationship Between the Severity of Hemolysis, Clinical Manifestations and Risk of Death in 415 Patients With Sickle Cell Anemia in the US and Europe." *Haematologica* 98: 464–472.

Pakbaz, Z., M. E. Hildesheim, S. Alam, et al. 2011. "Serum Transferrin: An Independent Predictor of Mortality in Sickle Cell Anemia." *Blood* 118: 2126.

Pakdaman, R., and J. M. E. H. Chahine. 1996. "A Mechanism for Iron Uptake by Transferrin." *European Journal of Biochemistry* 236: 922–931.

Pires, I. S., K. Govender, C. J. Munoz, et al. 2021. "Purification and Analysis of a Protein Cocktail Capable of Scavenging Cell-Free Hemoglobin, Heme, and Iron." *Transfusion* 61: trf.16393. https://doi.org/10.1111/trf.16393.

Redinus, K., J. H. Baek, A. Yalamanoglu, et al. 2019. "An Hb-Mediated Circulating Macrophage Contributing to Pulmonary Vascular Remodeling in Sickle Cell Disease." *JCI Insight* 4: 1–16.

Reiter, C. D., X. Wang, J. E. Tanus-Santos, et al. 2002. "Cell-Free Hemoglobin Limits Nitric Oxide Bioavailability in Sickle-Cell Disease." *Nature Medicine* 8: 1383–1389.

Rolf, J. M., A. Ohmizu, S. D. Latham, and P. Bhattacharya. 1996. "Manufacturing Process for the Production of Purified Transferrin. US Patent 5,744,586."

Rottman, G. A., K. Doi, O. Zak, R. Aasa, and P. Aisen. 1989. "Hyperfine Interactions of Iron-57 in Human Transferrin: An Endor Spectroscopic Study." *Journal of the American Chemical Society* 111: 8613–8618.

Schneider, C. A., W. S. Rasband, and K. W. Eliceiri. 2012. "NIH Image to ImageJ: 25 Years of Image Analysis." *Nature Methods* 9: 671–675.

Shore, P. M., B. J. Biemond, and R. Kesse-Adu, et al. 2024. "Phase 1 Study of the Safety and Pharmacokinetics of CSL889 (Hemopexin) in Adults With SCD." *Journal of Sickle Cell Disease* 1: 29–30.

Smith, M. A., P. L. R. Harris, L. M. Sayre, and G. Perry. 1997. "Iron Accumulation in Alzheimer Disease Is a Source of Redox-Generated Free Radicals." *Proceedings of the National Academy of Sciences* 94: 9866–9868.

Stites, S. W., M. E. Nelson, and L. J. Wesselius. 1995. "Transferrin Concentrations in Serum and Lower Respiratory Tract Fluid of Mechanically Ventilated Patients With COPD or ARDS." *Chest* 107: 1681–1685.

Tang, S., R. MacColl, and P. J. Parsons. 1995. "Spectroscopic Study of the Interaction of Aluminum Ions With Human Transferrin." *Journal of Inorganic Biochemistry* 60: 175–185.

Von Bonsdorff, L., H. Tölö, E. Lindeberg, T. Nyman, A. Harju, and J. Parkkinen. 2001. "Development of a Pharmaceutical Apotransferrin Product for Iron Binding Therapy." *Biologicals* 29: 27–37.

Wally, J., P. J. Halbrooks, C. Vonrhein, et al. 2006. "The Crystal Structure of Iron-Free Human Serum Transferrin Provides Insight Into Inter-Lobe Communication and Receptor Binding." *Journal of Biological Chemistry* 281: 24934–24944.

Welch, S., and A. Skinner. 1989. "A Comparison of the Structure and Properties of Human, Rat and Rabbit Serum Transferrin." *Comparative Biochemistry and Physiology Part B: Comparative Biochemistry* 93: 417–424.

Winterbourn, C. C. 1990. "Oxidative Reactions of Hemoglobin." *Methods in Enzymology* 186: 265–272.

Supporting Information

Additional supporting information can be found online in the Supporting Information section.